Novel synthesis, structural, linear and nonlinear optical properties of p-type kesterite nanosized Cu_2MnGeS_4 thin films

I. M. El Radaf[1,2] · H. Y. S. Al-Zahrani[3] · Ahmed Saeed Hassanien[4,5]

Abstract

This study presents the preparation of novel Cu_2MnGeS_4 thin films deposited on glass substrates, for the first time by an inexpensive spray pyrolysis technique. The crystal structure of the Cu_2MnGeS_4 samples was checked via the X-ray diffraction technique. The field-emission scanning electron microscope is used to investigate the surface morphology of the present films. Energy-dispersive spectroscopy has been employed to detect the compositional elemental percentage of thin films. Some structural parameters and defects, of the Cu_2MnGeS_4 samples, like the microstrain, the crystallite size, the dislocation density, and crystallites per unit surface area have been computed, studied and discussed. The experimental transmittance and reflectance spectra of the Cu_2MnGeS_4 samples have been measured to evaluate the linear and nonlinear optical parameters. The linear optical results indicate that Cu_2MnGeS_4 samples displayed a directly allowed optical transition and the optical energy gap values were reduced from 1.495 to 1.301 eV by increasing the thickness. Moreover, the dispersion parameters obtained and discussed via the Wemple-DiDomenico model. In addition, the nonlinear optical parameters of the Cu_2MnGeS_4 samples were computed and analysed. The hot-probe experiment indicates that the Cu_2MnGeS_4 films exhibited p-type conductivity.

1 Introduction

Nowadays, the research of material science is heading to produce a more efficient, easily fabricated, and low-cost absorber layer suitable for thin-film solar cells, using

✉ I. M. El Radaf
elradaf11b@gmail.com; i.radaf@qu.edu.sa

✉ Ahmed Saeed Hassanien
a.s.hassanien@gmail.com; ahmed.hassanien@feng.bu.edu.eg

1 Physics Division, Electron Microscope and Thin Films Department, National Research Centre, Dokki, Giza 12622, Egypt

2 Materials Physics and Energy Laboratory, College of Sciences and Art at ArRass, Qassim University, Ar Rass 51921, Saudi Arabia

3 Physics Department, Faculty of Science and Arts, King Abdulaziz University, Rabigh, Saudi Arabia

4 Engineering Mathematics and Physics Department, Faculty of Engineering at Shoubra, Benha University, Benha 11629, Egypt

5 Physics Department, Faculty of Science and Humanities in Afif Governorate, Shaqra University, Shaqra 11921, Saudi Arabia

efficient elements, earth-abundant and at the same time low-cost semiconductor materials. In the past, most of the published articles were concentrated on the CdTe and $CuInGaSe_2$ thin films as good absorber layers for solar cells. But because of the preparation methods that require high technology, complicated procedures or more expensive; whether these techniques are co-evaporation, sputtering, selenization, and some other non-vacuum ways like the electro-deposition, pulsed laser deposition and others [1–3], as well as the high price of these used elements and the toxicity of their some elements, make the researcher concentrated on fabricating a new family of materials. This family characterized by (1) their efficiency, (2) ease and availability of the possibilities to their preparation, (3) inexpensive or of lower costs, (4) earth-abundant, and (5) low toxicity.

This new family of materials is called kesterite materials, which are classified as p-type materials that have a larger absorption coefficient and lower bandgap. Therefore, they are used as new promising absorber layers for solar cells. Copper-based kesterite thin films, like Cu_2ZnSnS_4, $Cu_2ZnSnSe_4$, and Cu_2NiSnS_4, have attracted attention for their potential application in photovoltaic [4], owing to their high absorption coefficient, ideal bandgap, low toxicity, and high thermal stability [5–8]. The good

optoelectronic properties, efficiency, nontoxicity, and earth-abundant, as well as the lower prices of Cu, Zn, Sn, and S make the Cu_2ZnSnS_4 composition suitable for photovoltaic applications, where they can produce more electricity. The last articles displayed the importance of the CZTS films which can provide a solar cell with an efficiency to about 9.6% using the thermal evaporation technique [9] and the efficiency can be reached to 12.6% using the electrodeposition method [10].

The kesterite thin films of the quaternary Cu_2MnGeS_4 and its similar compositions are new semiconductor materials that have unique and distinctive properties, just like the Cu_2ZnSnS_4 thin films. This composition is crystallized either in the orthorhombic superstructure of a space group $Pmn2_1$, which is known as Wurtz-stannite or in the tetragonal structure of the space groups' ($I\,4\,2\,m$, $P\,4$ or $I\,\bar{4}$) structures [11, 12]. Moreover, $CuMnGe_4$ thin films are direct bandgap semiconductors characterized by their high absorption coefficient and adjustable bandgap that can be adjusted. Therefore, these distinctive Cu_2CoSnS_4, Cu_2FeSnS_4, Cu_2ZnSnS_4 and Cu_2MnGeS_4 films correspond positively with the solar spectrum. Therefore, these distinctive films correspond positively with the solar spectrum [13, 14]. Hence, they become suitable to produce a good absorber layer for solar cells. For these reasons, the films of these materials are considered fertile materials for future scientific solar and space researches [13–15].

Previous studies have displayed that there are no articles dealing with the manufacturing or characterization of the current novel Cu_2MnGeS_4 thin films. Therefore, the authors found it very difficult to compare their obtained results with previous ones. But to overcome this problem, the authors resorted to citing similar works, such as Cu_2ZnSnS_4, Cu_2MnSnS_4 and $Cu_2ZnGeSe_4$, especially since they have previously published works like this presented work. They have studied the structural, optical and optoelectronics properties of some similar thin films [16, 17].

The primary motivation behind this article was the authors' desire to complete their preparation and study of these compositions and their thin films. The authors have begun to study the quaternary polycrystalline Cu_2MnSnS_4 and $Cu_2ZnGeSe_4$ thin-film samples before and are currently studying Cu_2MnGeS_4 films, to reach the optimum composition and the best thickness of films that can be generalized for usages in photovoltaic and solar energy applications. Hence, this research aims to prepare homogeneous and high-quality thin films and then to study the structural, optoelectrical, linear and nonlinear optical properties. So, in this work, the authors present the novel fabrication of new absorber Cu_2MnGeS_4 thin films by spray pyrolysis technique for the first time. Then, they have investigated and discussed these properties.

2 Experimental details

High-quality Cu_2MnGeS_4 films have been fabricated successfully using an inexpensive spray pyrolysis technique via the reaction between high-purity 0.1 M copper chloride, 0.05 M manganese chloride, 0.05 M $GeCl_4$ and 0.2 M thioacetamide CH_3CSNH_2 as a source of copper, manganese, germanium and sulphur ions. A double-distilled water was used for the preparation of the Cu_2MnGeS_4 solution. The Cu_2MnGeS_4 solution was magnetically stirred at 60 °C for 1 h to get a uniform brown solution. The Cu_2MnGeS_4 solution was sprayed on the glass substrate via the spray pyrolysis technique according to the following conditions: the solution flow rate equal 20 ml/min, the substrate temperature equal 350 °C, the pressure of air equals 3 atm., and the distance between the nozzle and the substrate was adjusted to be 30 cm. The film thickness of the Cu_2MnGeS_4 thin films was evaluated using an alpha-step D-500 stylus profilometer. In addition, the microstructural properties of the Cu_2MnGeS_4 films were examined via an X-ray diffraction technique type (X'Pert) with CuKα radiation, of wavelength 1.54106 Å. Moreover, X-ray diffraction is an appropriate way to well verify the formed phases and whether there is more than one phase or not, and besides, to examine the crystallinity/non-crystallinity nature of samples, too. The continuous scanning was operated at a slow scanning rate 1°/min and the applied time constant was small ≈ 1 s; besides, the applied powerful energy ≈ 8.042 keV. These conditions are enough to well investigate the synthesized films and detect any possible diffraction peaks, especially between the two diffraction angles (25°–35°). Consequently, X-ray diffraction diagrams give good and enough information about the formation nature of the film samples and the formed single Cu_2MnGeS_4 phase, as well as it is a cheap, easy, fast and highly reliable technique [18–20].

On the other hand, the field-emission electron scanning microscope, FE-SEM (Quanta Fe G 250), was used to examine the surface morphology of Cu_2MnGeS_4 thin films. This FE-SEM is equipped with a separate attachment of the energy-dispersive X-ray spectroscopy, EDAX, to investigate the elemental composition ratios of each film sample. The operated voltage during the scanning process of film samples was 20 kV. The magnification power of the SEM was enlarged to well examine the surface nature of films. It was focused on surface nature and the particle size on the surface of the present films and to analyse their compositional elements. Moreover, the transmittance (T) and reflectance (R) optical data of the sprayed Cu_2MnGeS_4 samples were recorded via a programmable double-beam spectrophotometer kind (SP, V-570, JASCO, Japan). It is worth mentioning that this computerized

spectrophotometer contains two cells, one specialized for the investigated sample and the other is for the reference material. Therefore, when the authors have recorded the spectrophotometric measurements of both T- and R-spectra in the studied spectral range (400–2500 nm), a glass slide of the same type of used substrates has been placed in the spectrophotometer cell, SP, as a reference material. And since, there is a software program installed on this used SP that performs these calculations, automatically and the result is the effect of the film material, only. Therefore, this computerized SP subtracts the effect of the reference material from the recorded values, and the result is because of the film, only. Hence, the represented T- and R-spectra have been computerized corrected.

3 Results and discussion

3.1 Structural analysis

The crystal structure of the Cu_2MnGeS_4 samples was checked by the X-ray diffraction instrument of (X'Pert) type and the obtained XRD charts are illustrated in Fig. 1. It is noted that the Cu_2MnGeS_4 film samples are polycrystalline and the indexed planes of these samples are in a good match with the standard data. In addition, the diffraction peaks of this pattern were positioned at the following (2θ): 27.46°, 29.15°, 36.54°

and 52.74° corresponding to the following diffraction planes (210), (120), (320), and (213), respectively. The analysis of X-ray data exhibits also that the prepared films belong to the orthorhombic crystal system. Moreover, the X-ray diffraction patterns do not show any other formed phase, which affirms a single phase of Cu_2MnGeS_4 is present, only; where the applied conditions able to detect any probable diffraction lines. Hence, the obtained results are in good consistency with the JCPDS No. 89-1953.

Furthermore, some structural parameters and defects of these polycrystalline Cu_2MnGeS_4 films, such as the crystallite size (D), dislocation density (δ), the number of crystallites per unit surface area N_C and the strain function (ε), were computed according to the below Scherrer formulas [21–24]:

$$D = \frac{0.9\lambda}{\beta \cos \theta} \tag{1}$$

$$\delta = \frac{1}{D^2} \tag{2}$$

$$N_C = \frac{t}{D^3} \tag{3}$$

$$\varepsilon_s = \frac{\beta \cos (\theta)}{4} \tag{4}$$

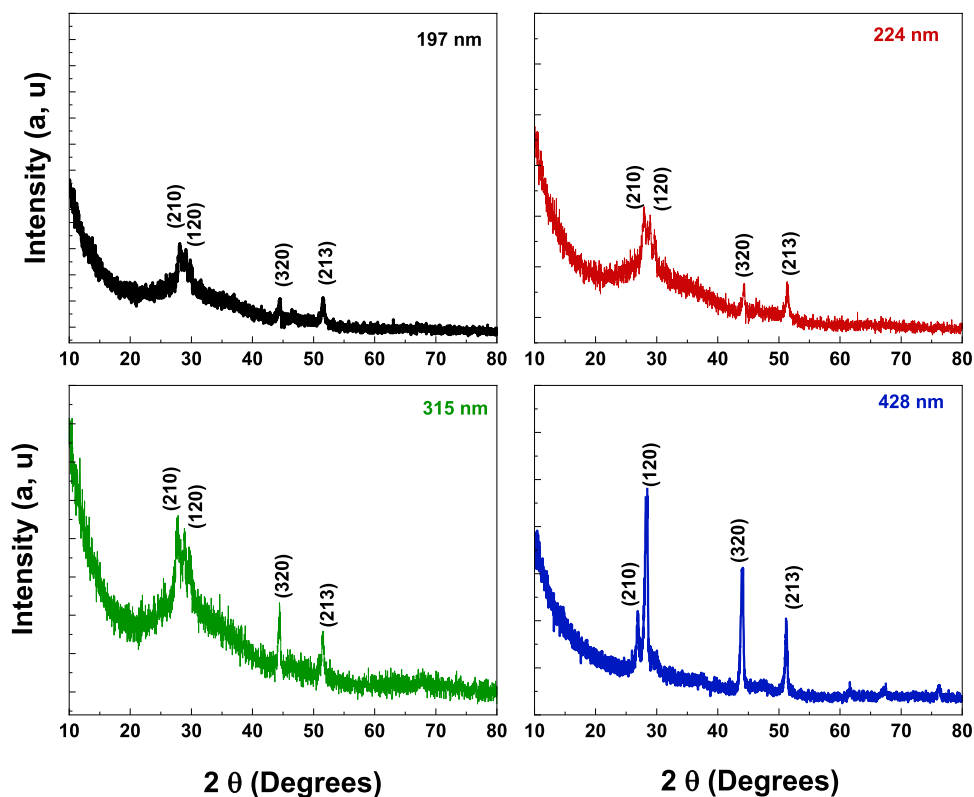**Fig. 1** X-ray diffraction patterns of the Cu_2MnGeS_4 thin films

Table 1 The average values of the grain size D, the microstrain function ε, the dislocation density δ and the number of crystallites of the Cu_2MnGeS_4 thin films

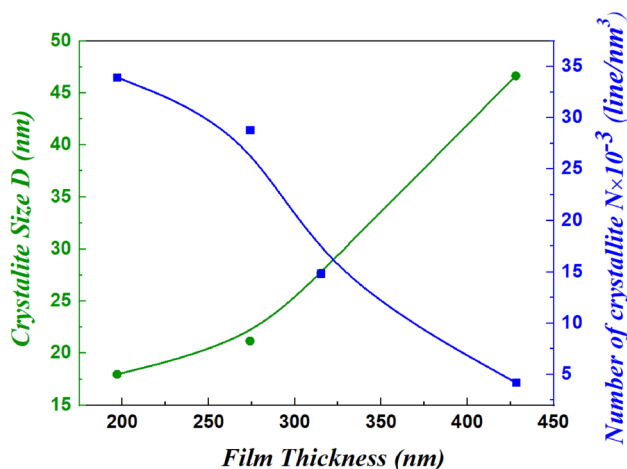| Thickness (nm)	D (nm)	$\varepsilon \times 10^{-3}$	$\delta \times 10^{-4}$ (nm)$^{-2}$	$N_C \times 10^{-3}$ (line/nm^3)
197	18.00	3.58	3.09	33.94
274	21.00	3.27	2.23	28.83
315	28.00	1.91	1.31	14.85
428	47.00	0.67	0.45	4.21

Fig. 2 The dependence of both the crystallite size D and the number of crystallite N on the thickness of the Cu_2MnGeS_4 thin films

Here, t and β are the film thickness of the Cu_2MnGeS_4 samples and the full width at the half maximum (FWHM), respectively. It is worthy to mention that to get the exact value of the broadening, β of film samples, the Gaussian distribution function at the full width at half maximum was used [25–27]. It is worth to mention that the β-values were computed for all observed diffraction peaks. Then, the values of D, δ, N_C, and ε_s were computed for all lines and the average values were considered. Table 1 reports these average computed values for the Cu_2MnGeS_4 thin films. The tabulated results in Table 1 demonstrate that increasing the film thickness of the Cu_2MnGeS_4 thin films is accompanied by an increase of the size of the crystallites (D), whilst it will reduce the size of the strain function (ε), number of crystallites per unit surface area NC and the dislocation density δ for the Cu_2MnGeS_4 films. Figure 2 shows the dependence of the crystallites size (D) and the number of crystallites per unit surface area N_C on the thickness of the Cu_2MnGeS_4 samples. It can be seen that the crystallinity improvement of films increases as the film thickness was increased. This improvement is owing to the agglomeration of small crystallites and the regularity of stacking atoms together and forming larger clusters, which leads to smaller

vacancies. Thereby, the values of the crystal defects of film samples decreased, as listed in Table 1 [14, 21–23].

In addition, the investigations of the field emission scanning electron microscope, FE-SEM, of the sprayed Cu_2MnGeS_4 samples are depicted in Fig. 3. It was focused on surface nature and the particle size on the surface of the present films and to analyse their compositional elements. Figure 3 shows these SEM micrographs and EDAX spectra. It can be seen from Fig. 3a, b, d that the present films have a good surface nature and of high homogeneity, as well as they are free crack. Moreover, the EDAX results of the Cu_2MnGeS_4 thin films, as shown in Fig. 3c and d, display a stoichiometric composition for the investigated films and confirm the presence of the Cu, Mn, Ge, and S peaks with an atomic ratio near to 2:1:1:4, respectively. It is worth mentioning that the scanning process of the film surface was carried out in different positions along the surface of films to well detect the constituent elemental percentages. The error in the detected compositional elements did not exceed $\pm 1\%$.

3.2 Linear optical analysis

In this work, the linear optical parameters of the Cu_2MnGeS_4 samples were computed by determining the transmittance (T) and reflectance (R) data. The dependence of the (T) and (R) on the λ, for the Cu_2MnGeS_4 samples, is depicted in Fig. 4a and b, respectively. It is worth mentioning that T- and R-spectra analysis for the polycrystalline Cu_2MnGeS_4 film samples displays that at lower wavelengths ($\lambda \leq 700$ nm) that the sum of their intensities is largely less than the unity ($T+R \ll 1$); but after this wavelength, it is almost equal the unity, where $T+R \approx 1$ for all films. This indicates that at higher wavelengths in the NIR-region the absorption nature of films becomes very small. Moreover, the intensity of T-spectra decreases, whilst that of R-spectra increases with the increasing thickness of Cu_2MnGeS_4 thin films along all the studied spectra. This is almost owing the increased absorption of the samples, as it will be observed in the next figure. Similar results have been observed by Al-Zahrani (2020) when studying the optical properties of Cu_2CoSnS_4 thin films [14, 16]

3.2.1 Absorption coefficient and skin depth

The absorption coefficient α of the Cu_2MnGeS_4 samples deposited at a various thickness (197 nm, 274 nm, 315 nm and 428 nm) was evaluated through the following equation [28, 29]:

$$\alpha = \frac{1}{d} \ln \left[\frac{(1-R)^2}{2T} + \left(\frac{(1-R)^4}{4T^2} + R^2 \right)^{1/2} \right]. \quad (5)$$

Here, d denotes the film thickness. Therefore, using R and T measurements, it could obtain the absorption
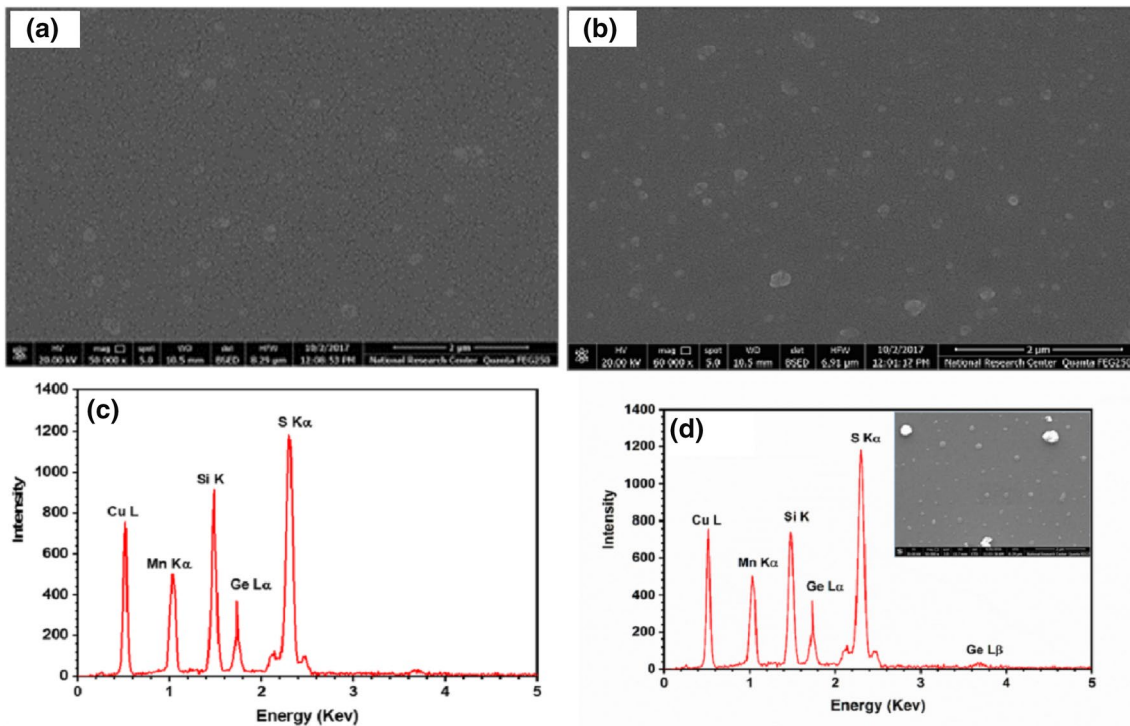
Fig. 3 **a** and **b** illustrate the Fe-SEM micrographs, whilst **c** and **d** depict the EDAX spectra of the two film samples of lower and higher thicknesses of the polycrystalline Cu_2MnGeS_4 film samples (197 nm and 428 nm), respectively, as representative examples

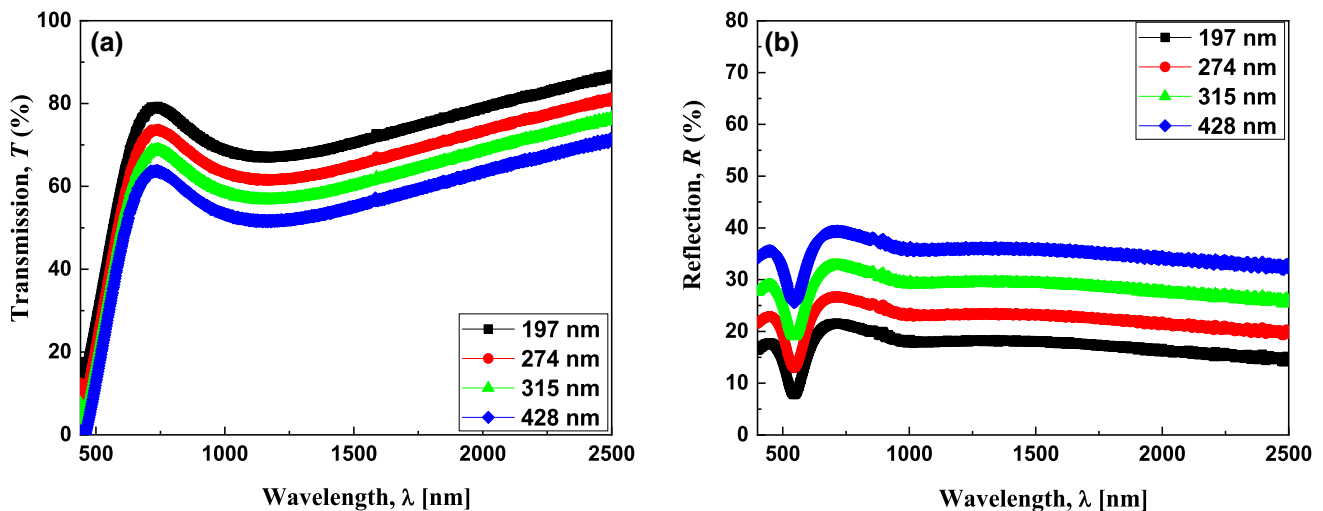**Fig. 4** Both the **a** transmittance and **b** reflectance spectra of the polycrystalline Cu_2MnGeS_4 thin films under investigations

coefficient spectra. Figure 5a illustrates the variation of α with the λ for the Cu_2MnGeS_4 samples. This figure displays also that the magnitudes of the absorption coefficient increased with the increasing thickness of films. From this figure, it can be observed that the absorption coefficient increases slightly with increasing film thickness. The reason is due to the improvement of the crystallinity of the polycrystalline Cu_2MnGes_4 thin films, which is confirmed also from the obtained values of the crystallite size of the present nanosized Cu_2MnGes_4 film samples (Please see Table 1). Where, the larger the thickness, the better the degree of crystallization of films. Consequently, there is an improvement of the stacking of the layers of the film, the closer the atoms are to each other, with a reduction
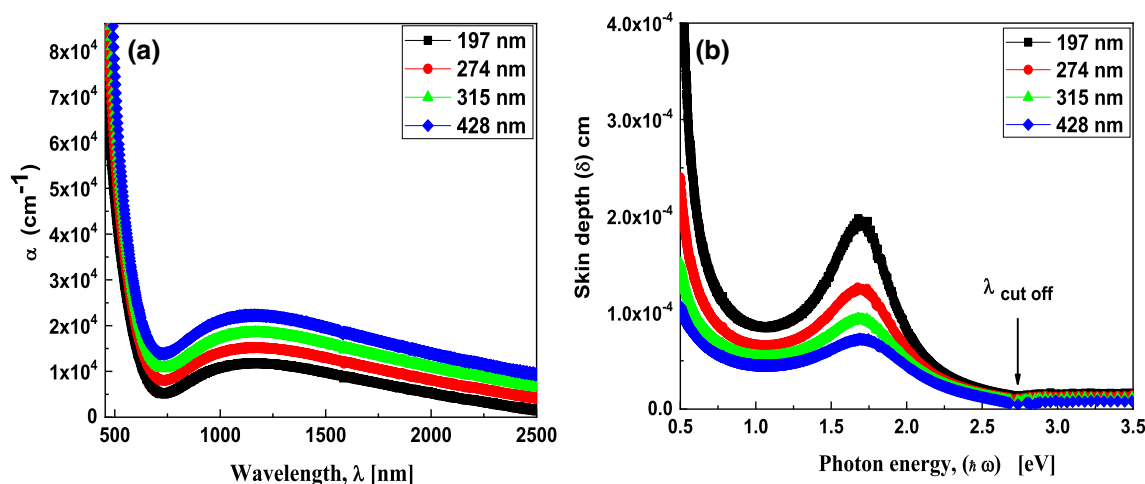
Fig. 5 The dependence of the spectra of **a** absorption coefficient on the wavelength and **b** the skin depth δ on the photon energy $h\nu$, for the Cu_2MnGeS_4 thin films of different thicknesses

in the disorders of atoms, and the diminished the existing vacancies [30–32]. Thereby, this led to an increase in the absorption of the film for the incident electromagnetic waves upon the film sample.

On the other hand, there is a crucial optical parameter that should be studied here because of it has great importance, it is the skin depth. Skin depth (δ) is the thickness at which the optical photon intensity turns out to equal ($1/e$) of its value on the surface of the film. The value of δ depends on two main parameters, they are the photon frequency and the conductivity of the film, where it inversely proportional to both. Therefore, the optical bandgap energy will strongly depend on this parameter, where the greater the skin depth, the lower the narrower of the forbidden bandgap and vice versa [18, 33]. The skin depth, δ, of the Cu_2MnGeS_4 thin films at different thicknesses (197 nm, 274 nm, 315 nm and 428 nm) has been evaluated via the below relation [34, 35]:

$$\delta = \frac{1}{\alpha}. \tag{6}$$

The variation of the δ of the Cu_2MnGeS_4 samples with the photon energy ($h\nu$) is displayed in Fig. 5b. It is noted that the skin depth of the Cu_2MnGeS_4 thin films was decreased with increment of the photon energy until it arrived at the cut-off wavelength. The value of the cut-off energy, $E_{\text{cut-off}}$, of the Cu_2MnGeS_4 samples was about 2.73 eV and the value of the $\lambda_{\text{cut-off}}$ was about 454 nm. As it is observed here that the value of the cut-off energy is relatively intermediate value as the values of E_g as it will be discussed later. Furthermore, the δ values of the Cu_2MnGeS_4 films are found to decrease with the increment of the film thickness. This is owing to the inversely proportional relationship between the skin depth and the absorption coefficient [14, 18, 36].

3.2.2 Absorption index and energy gap evaluating

The absorption of light waves and the optical dielectric parameters of any medium depend mainly on the absorption index [37, 38]. This optical index (k), for the nanosized Cu_2MnGeS_4 film samples, was evaluated by the below equation [39, 40]:

$$K = \frac{\alpha\lambda}{4\pi}. \tag{7}$$

The spectral variations of k with λ for the Cu_2MnGeS_4 films of different film thicknesses are displayed in Fig. 6a. It can be observed from this plot that all the curves exhibit the same trend, where the absorption index (k) very slightly increases with the increment of the film thickness. Generally, the k values are very small and decreases dramatically from about 0.30 at lower wavelengths (less than 500 nm) to become less than 0.05 in the visible region. Moreover, almost after 1000 nm, the k values more decreased to reach values less than 0.035. This means that at lower photon energies, the scattering or absorption of the electromagnetic waves is reduced and the conductivity is more increased.

On the other side, and according to the Tauc's relation, the bandgap energy of the Cu_2MnGeS_4 thin films was computed by [41–43]:

$$\alpha h\nu = A\left(h\nu - E_g\right)^r. \tag{8}$$

Here, A is some constant and r is another constant; it has the values of 2 and 1/2 for indirect allowed and directly allowed transitions, respectively. In this work, the proper fit was found for $r = 1/2$ which implies the state of allowed direct transition of the Cu_2MnGeS_4 thin films. Figure 6b displays the plot of $(\alpha h\nu)^2$ against $h\nu$ for the polycrystalline
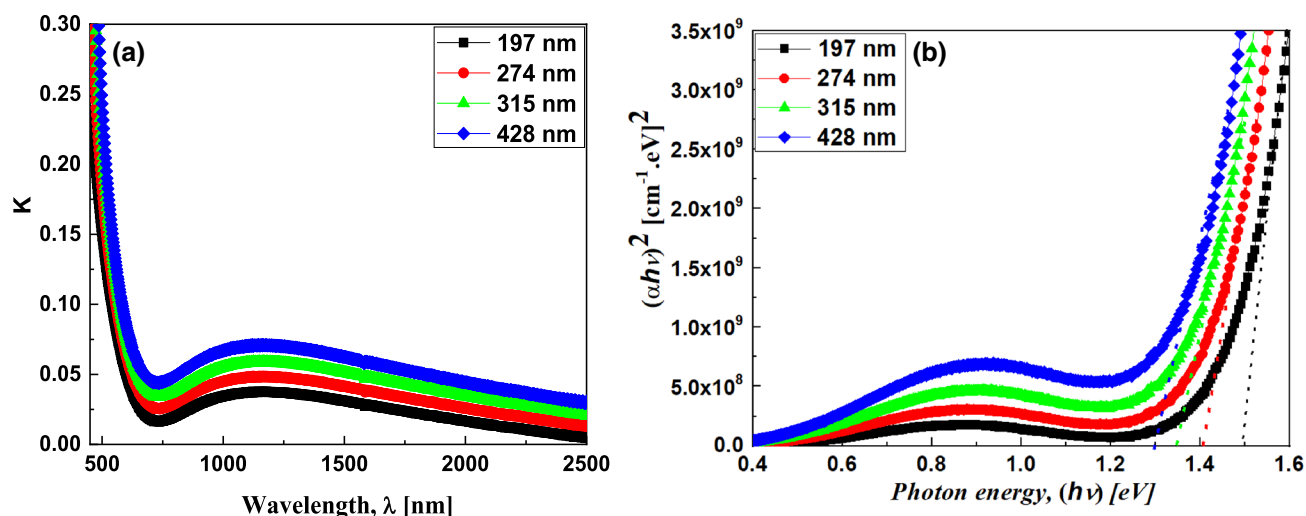
Fig. 6 a The absorption index as a function of wavelength and **b** the plotting of $(\alpha h \nu)^2$ versus the photon energy $h\nu$, for the quaternary Cu_2MnGeS_4 thin films

Cu_2MnGeS_4 films. From this plot, it can evaluate the values of the direct energy gap, which are tabulated in Table 2. The direct energy gap values for the Cu_2MnGeS_4 samples decreased from 1.495 to 1.301 eV as the film thickness was increased. This decrease in the values of the optical bandgap energy, E_g, can be also attributed to the improvement of the crystallinity of the polycrystalline Cu_2MnGeS_4 thin films, as mentioned before. Where the greater the thickness, the improving the crystallization of films was. Where the atoms become closer to each other, the stacking of the layers of the film becomes better, thereby there is a reduction in the disorders of atoms which led to diminishing the existing vacancies [29–31]. Consequently, the energy bandgap slightly decreases from 1.495 to 1.301 eV as the film thickness increases from 197 to 428 nm. These results are in good match with similar published work by Al-Zahrani [14] and El Saeedy, et al. [44], when they studied the optical properties of Cu_2CoSnS_4 and Cu_2FeSnS_4 thin films, respectively.

Moreover, the interrelationship between the estimated values of the microstructural parameters (crystallite size and microstrain function) and the obtained optical bandgap energy values should be discussed here. As a result of increasing the film thickness, it was found that the crystallite size increased. This in turn leads to the improvement of the crystallization of the films. Therefore, this crystallization

improvement led to a decrease of the strain function, as computed and then tabulated in Table 1. On the other side, and as it is known, the stress is directly proportional to the strain and the proportionality is Young's Modulus, Y. Hence, the improvement of the crystallization of films leads to a decrease in the internal stress and the lattice deformation of the crystal lattice, too (as listed in Table 1). Thus, the electrons of atoms become freer and could move easily and move from the valence band, VB, to the conduction band, CB. This only happens if the width of the bandgap is reduced, too, or the increasing of the localized states formed in the forbidden gap due to the disorder of S-atoms [8, 14, 29, 44]. This is indeed was obvious, as the optical bandgap energy values decreased as the film thickness increased, as reported in Table 2. Furthermore, the film conductivity has increased due to the shrinkage of the bandgap value, which will be discussed later in Sect. 3.2.5. Similar results have been observed by several authors when studying the optical properties of Cu_2CoSnS_4 and Cu_2FeSnS_4 thin films [14, 44].

3.2.3 Refractive index and dispersion analysis

The importance of the refractive index is owing to the extent of the influence of matter by electromagnetic waves. The value of the refractive index is a variable parameter, where

Table 2 The values of the energy gap and the oscillator parameters for the Cu_2MnGeS_4 thin films

Thickness (nm)	E_g (eV)	E_d (eV)	E_o (eV)	n_o	ε_s	f (eV)^2
197	1.495	5.442	3.451	1.605	2.577	18.780
274	1.425	5.823	3.379	1.650	2.723	19.676
315	1.345	6.481	3.260	1.729	2.988	21.128
428	1.301	7.280	3.109	1.828	3.342	22.633

it depends on the wavelength of the electromagnetic wave. In general, the higher the density of the material, the greater the refractive index of that material, which means a decrease in the speed of light or decreasing the spreading of electromagnetic waves through this material. The refractive index consists of two parts; the real and imaginary parts. When light propagates through an absorbent material, the refractive index of that substance can be described by a complex number. The real part (n) expresses the refraction of incident light by the matter, whilst the imaginary part of this complex number expresses the attenuation of the incident light waves. According to Kramer–Kroning's formula, the real part of the refractive index (n) of the Cu_2MnGeS_4 films could be computed via this form [45–47]:

$$n = \frac{1+R}{1-R} + \left(\frac{4R}{(1-R)^2} - k^2\right)^{1/2}. \tag{9}$$

Here, R and T are the reflectance and transmittance of the Cu_2MnGeS_4 films deposited at different film thicknesses. Using Eq. (9), it could obtain the spectral variation of (n) as a function of (λ), then it is depicted in Fig. 7a. The analysis of this curve illustrated that the (n) of the Cu_2MnGeS_4 samples has an anomalous dispersion in $\lambda < 715$ nm and there is a normal dispersion in $\lambda > 715$ nm. In addition, the n values were increased with the increment of the film thickness. This increase is also attributed to the improvement in the crystallization of the films, the atoms become closer to each other, and thereby their agglutination and arrangement become better. Thus, this is what was occurred and led to an increase in the refractive index with the increase of the film thickness [22, 34]. This behaviour shows a close agreement with the contribution of the electronic transition in the Cu_2MnGeS_4 thin films that

can lead to some remarkable changes in the optical parameters. Some previous works have been published before and had almost compatible results with those obtained [14, 16, 44].

Moreover, the dispersion parameters of the Cu_2MnGeS_4 samples have a greater role in identifying the materials for their usages in the different optoelectronic applications. Therefore, the dispersion parameters of the Cu_2MnGeS_4 samples should be computed and studied. The single oscillator model of Wemple-DiDomenico was used to study these parameters, via utilizing these formulas [48, 49]:

$$n^2 = 1 + \frac{E_o E_d}{E_o^2 - (h\upsilon)^2}. \tag{10}$$

Here, E_d represents the dispersion energy and E_o the single oscillator energy. The values of E_o and E_d for the Cu_2MnGeS_4 films were calculated according to Eq. (10) and by plotting a graph between the $(n^2 - 1)^{-1}$ versus the $(h\upsilon)^2$ as demonstrated in Fig. 7b. The graph yields a straight line; its slope and intercept give $(E_o E_d)^{-1}$ and (E_o/E_d), respectively. Moreover, the dependences of E_o and E_d on the thickness of the Cu_2MnGeS_4 samples are given in Fig. 8. It is noted from this plot that the E_d values increased with the increasing film thickness, whilst the E_o exhibits the reverse manner of E_d. In addition, the static dielectric constant ε_s, the static refractive index n_o and the oscillator strength f of the Cu_2MnGeS_4 films were evaluated according to these presented relations [50–53]:

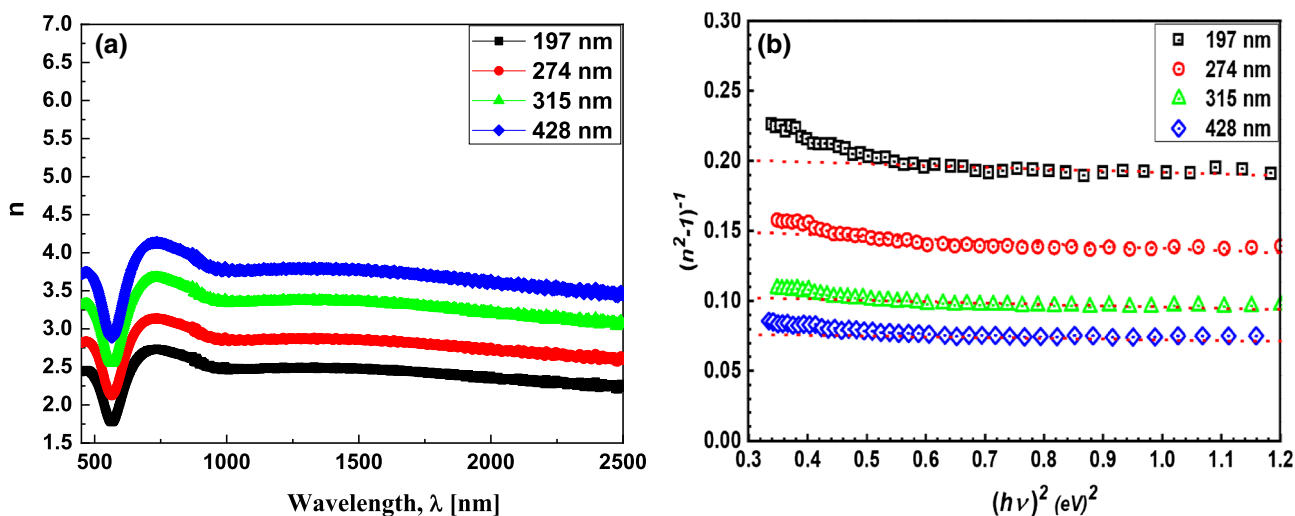$$f = E_o E_d \tag{11}$$

$$n_o = \sqrt{1 + \frac{E_d}{E_o}} \tag{12}$$

Fig. 7 **a** The refractive index as a function of wavelength and **b** the dependence of $\left(n^2 - 1\right)^{-1}$ on $(h\upsilon)^2$, for the Cu_2MnGeS_4 thin films under study
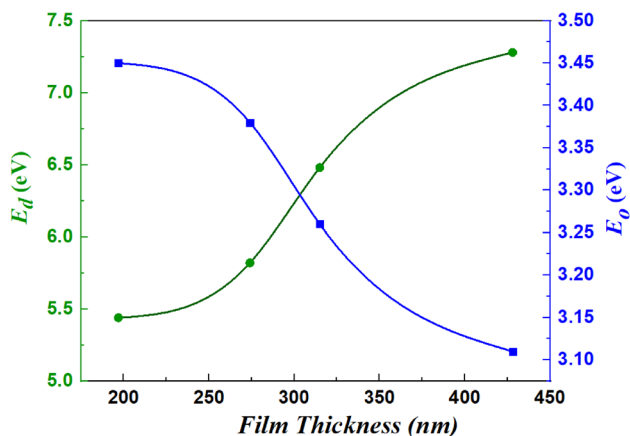
Fig. 8 The variation of the E_o and E_d with the film thickness of the Cu$_2$MnGeS$_4$ thin films

$$\varepsilon_s = n_o^2 \qquad (13)$$

Table 2 displays the magnitudes of the static dielectric constant ε_s, the static refractive index n_o and the oscillator strength f of the Cu$_2$MnGeS$_4$ thin films. It is noted that by increasing the film thickness the magnitudes of the f, n_o and ε_s were increased. Whereas, these parameters are highly dependent on the refractive index values, which increased as the film thickness increased. Therefore, the increased values of these parameters (f, n_o and ε_s) are attributed to this increase in the refractive index values, which resulted from the improvement of the crystallization of films, the approach of atoms to each other and their arrangement in a more stacking way, as well as minimizing the crystal defects and the vacancies [14, 30, 44]. In literature, comparable results have been reported when the dispersion parameters of Cu$_2$CoSnS$_4$ and Cu$_2$FeSnS$_4$ thin films have been studied [14, 44].

3.2.4 Optical dielectric constants

According to the n and k calculations, the real part of dielectric constant ε_1 and the imaginary part of the dielectric constant ε_2 of the Cu$_2$MnGeS$_4$ samples were computed by [54, 55]:

$$\varepsilon_1 = n^2 - k^2 \qquad (14)$$

$$\varepsilon_2 = 2nk \qquad (15)$$

Figure 9a and b depicts that the values of ε_1 and ε_2 were increased with increment of the film thickness. In addition, the performance displays a good optical response of the dielectric constants with the lattice parameter and particle size of Cu$_2$MnGeS$_4$ thin films. As discussed before, these dielectric parameters are also dependent upon the refractive index values, which increased as film thickness was increased due to the improvement of the film crystallization and reduction of the atomic interplanar distances, as well as minimization of the crystal defects and the vacancies [20, 30].

3.2.5 Optical and electrical conductivity evaluation

In this work, the optical conductivity σ_{opt} and electrical conductivity σ_e of the sprayed Cu$_2$MnGeS$_4$ films were computed via the below expressions [29, 56]:
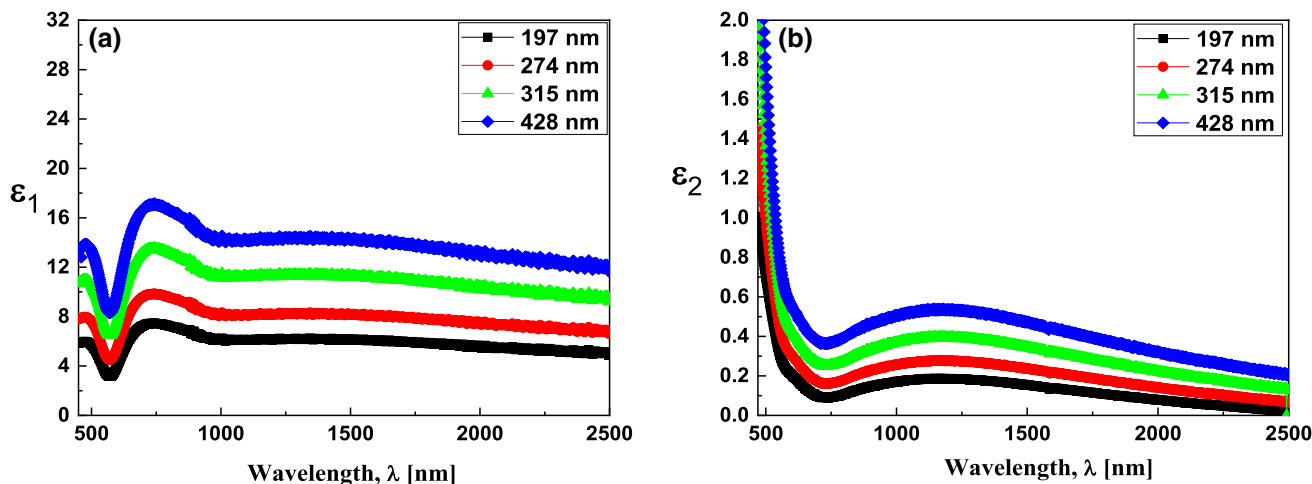
$$\sigma_{opt} = \frac{\alpha n c}{4\pi} \qquad (16)$$

Fig. 9 The variation of the **a** real dielectric constant and **b** the imaginary dielectric constant, as functions of photon energy, for the Cu$_2$MnGeS$_4$ films

$$\sigma_e = \frac{2\lambda\sigma_{opt}}{\alpha} \tag{17}$$

Here, (c) represents the speed of light. Figure 10a depicts the variant of the σ_{opt} with the $h\nu$ for the Cu_2MnGeS_4 samples. It is noted from this figure that the magnitudes of the σ_{opt} were increased with the increment of the film thickness and the photon energy; this trend could be interpreted as a result of increasing of electrons excitation with rising the photon energy. Furthermore, Fig. 10b illustrates the variations of the (σ_e) versus the ($h\nu$) for the Cu_2MnGeS_4 samples. It can be seen from this curve that the electrical conductivity for the Cu_2MnGeS_4 samples increases with the increasing film thickness and decreases as the photon energy was increased. The increased values of both σ_{opt} and σ_e are ascribed to reducing the values of crystal defects, the stress, and the lattice deformations. The decrease of these factors makes the conductivity become greater, the electromagnetic waves travel faster, and electrons move more freely and with higher speeds, i.e. the conductivities increase. Previous works have reported similar results for the current studied film samples [14, 44].

3.3 Nonlinear optical characterization

Nonlinear optical parameters have been paid more attention in recent articles for all investigated material due to their important applications in electro-optic modulators, optical switching devices, optical circuits and optical signal processing. There are two important nonlinear parameters that can be determined by utilizing semi-empirical relations which depend mainly on the film's refractive indices. The parameters are the third-order nonlinear susceptibility $\chi^{(3)}$ and the nonlinear refractive index n_2.

In this study, the magnitudes of the $\chi^{(3)}$ and n_2 for the Cu_2MnGeS_4 films were computed by the below Miller's formulas [57–61]:

$$\chi^{(3)} = B\left[\frac{n_0^2 - 1}{4\pi}\right]^4 \tag{18}$$

$$n_2 = \frac{12\pi\chi^{(3)}}{n_0} \tag{19}$$

Here, n_0 presents the values of the static refractive index, and B is a constant factor equal 1.7×10^{-10} esu. Table 3 displays the values of $\chi^{(3)}$ and n_2 corresponding to different thicknesses for the Cu_2MnGeS_4 samples. Figure 11 depicts that the values of $\chi^{(3)}$ and n_2 of the Cu_2MnGeS_4 samples were enlarged with the increment of the film thickness. The increase in the values of $\chi^{(3)}$ and n_2 is also ascribed to the increase in the values of the static refractive index, n_o, which consequently came as a result of the increase in the linear refractive index, n due to the improvement of the film crystallization and the decrease in the values of the crystal defects, stresses, and lattice deformations occurring within the film textures. Some previous

Table 3 The nonlinear optical parameters for the Cu_2MnGeS_4 thin films of different thicknesses

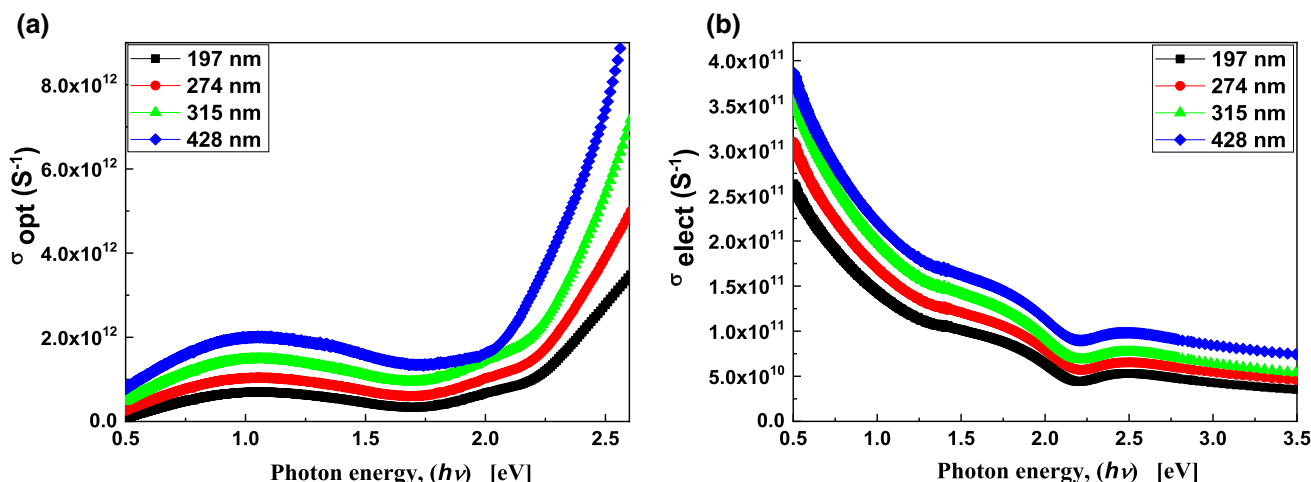| Thickness (nm)	$\chi^{(3)} \times 10^{-13}$ esu	$n_2 \times 10^{-12}$ esu
197	0.422	0.99
274	0.60	1.37
315	1.06	2.30
428	2.05	4.22

Fig. 10 The dependence of the **a** optical conductivity and **b** the electrical conductivity as functions of photon energy, for the Cu_2MnGeS_4 thin films of different thicknesses
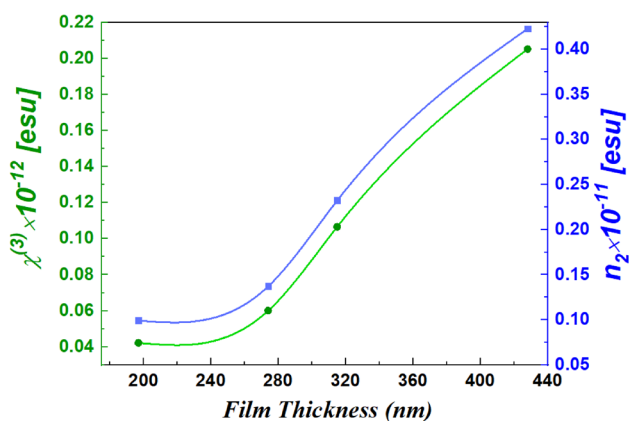
Fig. 11 The dependence of third-order nonlinear optical susceptibility $\chi^{(3)}$ and nonlinear refractive index n_2 on the thickness for the Cu_2MnGeS_4 thin films

works of similar thin films reported comparable results for these nonlinear optical parameters [14, 16, 44].

3.4 Determination of the semiconductor type

The hot-probe method was employed to check the semiconducting type of the polycrystalline Cu_2MnGeS_4 thin films using the two-probe technique, where the two probes were joined to a sensitive digital multimeter. The experiment occurred by joining the cold probe to the negative port and the hot probe was joined to the positive connection. The experiment displays a positive voltage is gained in the case of n-type semiconductor and a negative voltage on the multimeter which reveals a p-type semiconductor [62, 63]. In this work, the applied method on the Cu_2MnGeS_4 films is displayed in Fig. 12. The experiment displays a negative voltage on a multimeter, which indicates that the Cu_2MnGeS_4 films reveal the p-type conductivity.

4 Conclusion

In this work, an inexpensive spray pyrolysis procedure was employed to synthesis polycrystalline nanosized Cu_2MnGeS_4 thin films of different thicknesses (197 nm, 274 nm, 315 nm and 428 nm). The film samples were deposited on precleaned glass substrate of good quality and of high transmittance. The XRD results presented that the Cu_2MnGeS_4 samples are polycrystalline with tetragonal structure and no other formed phases. Increasing the film thickness leads to improving the crystallinity of films and increasing of the crystallite size from 18.00 to 47.00 nm, whilst their microstrain decreased from 3.58×10^{-3} to
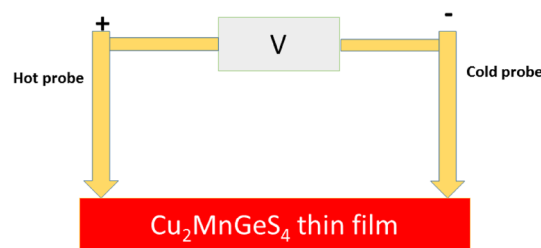

Fig. 12 Schematic diagram of the hot-probe experiment for determining the semiconducting type of the Cu_2MnGeS_4 thin films

0.67×10^{-3}. The EDAX results have confirmed the stoichiometry of the chemical composition of the Cu_2MnGeS_4 thin films, where the elemental ratio is 2:1:1:4.

The transmittance and reflectance measurements are utilized to study the optical properties and parameters. The optical results displayed that the skin depth and the direct optical band gap of the Cu_2MnGeS_4 films were found to decrease with the increasing film thickness, whilst the absorption coefficient has a reciprocal behaviour. The optical bandgap arose due to the directly allowed transition and decreased from 1.495 to 1.301 eV. The single oscillator model proposed by Wemple-DiDomenico was employed to study and discuss the dispersion energies and some other parameters for the nanostructural Cu_2MnGeS_4 thin films. It was found that the dispersion energy, static refractive index, static dielectric constant and the oscillator strength of the Cu_2MnGeS_4 films slightly increased as the film thickness increased, whilst the oscillator energy decreases.

The optical conductivity and the determined non-linear optical parameters of the Cu_2MnGeS_4 samples, such as the third-order susceptibility and non-linear refractive index, were increased with the increasing film thickness. The hot-probe technique was applied to the Cu_2MnGeS_4 films and displays negative voltage on a multimeter, which shows that the Cu_2MnGeS_4 films are p-type semiconductors.

References

1. J. Bi, J. Ao, M.-J. Jeng, L. Yao, S. Gao, G. Sun, Q. He, Z. Zhou, Y. Sun, Y.-L. Xiao, L.-B. Chang, Three-step vapor Se/N$_2$/vapor Se reaction of electrodeposited Cu/In/Ga precursor for preparing CuInGaSe$_2$ thin films. Solar Energy Mater. Solar Cells **159**, 352–361 (2017)
2. J. Der Wu, L.T. Wang, C. Gau, Synthesis of CuInGaSe$_2$ nanoparticles by modified polyol route. Solar Energy Mater. Solar Cells **98**, 404–408 (2012)
3. R. Chandran, A. Kumar Behera, A. Mallik, A novel CISe/Ga-Se two-step stack approach to electrodeposit photovoltaic quality Cu-poor CuInGaSe$_2$ thin films. Mater. Lett. **252**, 244–247 (2019)
4. H. Katagiri, K. Jimbo, M. Tahara, H. Araki, K. Oishi, The influence of the composition ratio on CZTS-based thin film solar cells, MRS Online Proc. Libr. Arch. 1165 (2009).

5. A. Weber, H. Krauth, S. Perlt, B. Schubert, I. Kötschau, S. Schorr, H.W. Schock, Multi-stage evaporation of Cu_2ZnSnS_4 thin films. Thin Solid Films **517**, 2524–2526 (2009)

6. X. Liu, Y. Feng, H. Cui, F. Liu, X. Hao, G. Conibeer, D.B. Mitzi, M. Green, The current status and future prospects of kesterite solar cells: a brief review. Prog. Photovolt. Res. Appl. **24**, 879–898 (2016)

7. F. Zhou, Xu Fangqin Zeng, F.L. Liu, N. Song, C. Yan, Pu Aobo, J. Park, K. Sun, X. Hao, Improvement of Jsc in Cu_2ZnSnS_4 solar cell by using a thin carbon intermediate layer at Cu_2ZnSnS_4_Mo interface. ACS Appl. Mater. Interfaces **7**(41), 22868–22873 (2015)

8. D. Chen, N.M. Ravindra, Electronic and optical properties of Cu_2ZnGeX_4 (X = S, Se and Te) quaternary semiconductors. J. Alloys Compd. **579**, 468–472 (2013)

9. A. Ziti, B. Hartiti, H. Labrim, S. Fadili, H.J. Tchognia Nkuissi, A. Ridah, M. Tahri, P. Thevenin, Effect of copper concentration on physical properties of CZTS thin films deposited by dip-coating technique. Appl. Phys. A **125**, 10 (2019)

10. M. Farinella, R. Inguanta, T. Spanò, P. Livreri, S. Piazza, C. Sunseri, Electrochemical deposition of CZTS thin films on flexible substrate. Energy Proc. **44**, 105–110 (2014)

11. Ch Power, E. Moreno, E. Quintero, D. Rivero, M. Quintero, C. Rincon, J.A. Henao, M.A. Macıas, Raman spectra study on Cu_2MnGeS_4 magnetic quaternary semiconductor with orthorhombic wurtz-stannite crystal structure. Phys. Status Solidi B **253**(2), 335–339 (2016)

12. M. Quintero, J. Marquina, E. Quintero, E. Moreno, S. Alvarez, C. Rincon, P. Grima, P. Bocaranda, D. Rivero, J.A. Henao, M.A. Macıas, X-ray diffraction analysis of stannite, wurtz-stannite and pseudo-cubic quaternary compounds by Rietveld method. Revista Mexicana de Física **60**, 168–175 (2014)

13. L. Tan, Y. Zhang, Y. Chena, Y. Chen, Homogeneous $Cu_2ZnSnSe_4$ nanocrystals/graphene oxide nanocomposites as hole transport layer for polymer solar cells. Chem. Phys. Lett. **622**, 1–8 (2015)

14. H.Y.S. Al-Zahrani, Synthesis, optical and optoelectrical analysis of the Cu_2CoSnS_4 thin films as absorber layer for thin-film solar cells. J. Mater. Sci. (2020). https://doi.org/10.1007/s10854-020-03252-7

15. E. Honig, H.-S. Shen, G.-Q. Yao, K. Doverspike, R. Kershaw, K. Dwight, A. Wold, Preparation and characterization of $Cu_2Znl_xMnxGeS_4$. Mater. Res. Bull. **23**, 307–312 (1988)

16. A.S. Hassanien, I.M. El Radaf, Optical characterizations of quaternary Cu_2MnSnS_4 thin films Novel synthesis process of film samples by spray pyrolysis technique. Phys. B **585**, 412110 (2020)

17. I.M. El Radaf, Structural, optoelectrical, linear, and nonlinear optical characterizations of the $Cu_2ZnGeSe_4$ thin films. J. Mater. Sci. (2020) 1–10.

18. A.S. Hassanien, A.A. Akl, Influence of composition on optical and dispersion parameters of thermally evaporated non-crystalline $Cd_{50}S_{50-x}Se_x$ thin films. J. Alloys Compd. **648**, 280–290 (2015)

19. A.S. Hassanien, A.A. Akl, A.H. Sáaedi, Synthesis, crystallography, microstructure, crystal defects, and morphology of $Bi_xZn_{1-x}O$ nanoparticles prepared by sol–gel technique. CrystEngComm **20**, 1716–1730 (2018)

20. A.S. Hassanien, A.A. Akl, X-ray studies: CO_2 pulsed laser annealing effects crystallography, microstructure and crystal defects vacuum deposited nanocrystalline ZnSe thin films. CrystEngComm **20**, 7120–7129 (2018)

21. A.A. Akl, A.S. Hassanien, Microstructure and crystal imperfections of nanosized CdS_xSe_{1-x} thermally evaporated thin films. Superlattices Microstruct. **85**, 67–81 (2015)

22. E.R. Shaaban, N. Afify, A. El-Taher, Effect of film thickness on microstructure parameters and optical constants of CdTe thin films. J. Alloys Compd. **482**, 400–404 (2009)

23. I.M. El Radaf, S.S. Fouad, A.M. Ismail, G.B. Sakr, Influence of Spray time on the optical and electrical properties of $CoNi_2S_4$ thin films. Mater. Res. Express. **5**, 46406 (2018)

24. C.-J. Kim, I.-S. Ahn, K.-K. Cho, S.-G. Lee, J.-K. Chung, Characteristics of $LiNiO_2$ thin films synthesized by Li diffusion on the surface oxidized epitaxial layer of Ni-alloy. J. Alloys Compd. **449**, 335–338 (2008)

25. A.A. Akl, A.S. Hassanien, Microstructural characterization of Al-Mg alloys by X-ray diffraction line profile analysis. Int. J. Adv. Res. **2**(11), 1–8 (2014)

26. A.S. Hassanien, A.A. Akl, Microstructure and crystal imperfections of nano-crystalline sprayed iridium oxides thin films. Phys. B **473**, 11–19 (2015)

27. A.A. Akl, S.A. Mahmoud, S.M. Al Shomar, A.S. Hassanien, Improving microstructural properties and minimizing crystal imperfections of nanocrystalline Cu_2O thin films of different solution molarities for solar cell applications. Mater. Sci. Semicond. Process. **74**, 183–192 (2018)

28. T.A. Hameed, A.R. Wassel, I.M. El Radaf, Investigating the effect of thickness on the structural, morphological, optical and electrical properties of $AgBiSe_2$ thin films. J. Alloys Compd. **805**, 1–11 (2019)

29. M.S. AlKhalifah, I.M. El Radaf, M.S. El-Bana, New window layer of $Cu_2CdSn_3S_8$ for thin film solar cells. J. Alloys Compd. **813**, 152169 (2020)

30. A.S. Hassanien, A.A. Akl, Optical characteristics of iron oxide thin films prepared by spray pyrolysis technique at different substrate temperatures. Appl. Phys. A **124**, 752 (2018)

31. N.F. Mott, E.A. Davis, *Electronic processes in non-crystalline materials* (Clarendon Press, Oxford, 1979)

32. M.M. El-Nahass, M.H. Ali, I.T. Zedan, Photoinduced changes in the linear and non-linear optical properties of $Ge_{10}In_{10}Se_{80}$ thin films. J. Non-Cryst. Solids **404**, 78–83 (2014)

33. S.S. Chiad, Optical characterization of NiO doped Fe_2O_3 thin films prepared by spray pyrolysis method. Intern. Lett. Chem. Phys. Astron. **6**, 50–58 (2015)

34. A.A. Yadav, M.A. Barote, P.M. Dongre, E.U. Masumdar, Studies on growth and characterization of $CdS_{1-x}Se_x$ (0.0 ≤ x ≤ 1.0) alloy thin films by spray pyrolysis. J. Alloys Compd. **493**, 179–185 (2010)

35. K.J. Tiwari, V. Vinod, A. Subrahmanyam, P. Malar, Growth and characterization of chalcostibite $CuSbSe_2$ thin films for photovoltaic application. Appl. Surf. Sci. **418**, 216–224 (2017)

36. A.S. Hassanien, A.A. Akl, Optical characterizations and refractive index dispersion parameters of annealed TiO_2 thin films synthesized by RF-sputtering technique at different flow rates of the reactive oxygen gas. Phys. B **576**, 411718 (2020)

37. A.S. Hassanien, Ishu Sharma, Optical properties of quaternary a-$Ge_{15-x}Sb_xSe_{50}Te_{35}$ thermally evaporated thin-films: refractive index dispersion and single oscillator parameters. Optik **200**, 163415 (2020)

38. A.S. Hassanien, I. Sharma, Band-gap engineering, conduction and valence band positions of thermally evaporated amorphous $Ge_{15-x}Sb_xSe_{50}Te_{35}$ thin films: influences of Sb upon some optical characterizations and physical parameters. J. Alloys Compd. **798**, 750–763 (2019)

39. A. Khan, M. Shkir, M.A. Manthrammel, V. Ganesh, I.S. Yahia, M. Ahmed, A.M. El-Toni, A. Aldalbahi, H. Ghaithan, S. AlFaify, Effect of Gd doping on structural, optical properties, photoluminescence and electrical characteristics of CdS nanoparticles for optoelectronics. Ceram. Int. **45**, 10133–10141 (2019)

40. M. Shkir, A. Khan, A.M. El-Toni, A. Aldalbahi, I.S. Yahia, S. AlFaify, Structural, morphological, opto-nonlinear-limiting studies on Dy:PbI_2/FTO thin films derived facilely by spin coating technique for optoelectronic technology. J. Phys. Chem. Solids **130**, 189–196 (2019)

41. S. Hamrouni, M.S. AlKhalifah, M.S. El-Bana, S.K. Zobaidi, S. Belgacem, Deposition and characterization of spin-coated n-type ZnO thin film for potential window layer of solar cell. Appl. Phys. A. **124**, 555 (2018)

42. A.M. Al-Baradi, M.M. El-Nahass, A.M. Hassanien, A.A. Atta, M.S. Alqahtani, A.O. Aldawsari, Influence of RF sputtering power on structural and optical properties of Nb_2O_5 thin films. Optik **168**, 853–863 (2018)

43. A.S. Hassanien, K.A. Aly, A.A. Akl, Optical properties of thermally evaporated ZnSe thin films annealed at different pulsed leaser powers. J. Alloys Compd. **685**, 733–742 (2016)

44. H.I. El Saeedy, H.A. Yakout, M.T. Elsayed, Fabrication and growth of linear and nonlinear optical behavior of Cu_2FeSnS_4 spherical nanostructured thin films. Appl. Phys. A **126**, 281 (2020)

45. T.A. Hameed, I.M. El Radaf, H.E. Elsayed-Ali, Characterization of $CuInGeSe_4$ thin films and $Al/n–Si/p–CuInGeSe_4/Au$ heterojunction device. J. Mater. Sci. **29**, 12584–12594 (2018)

46. I.S. Yahia, I.M. El Radaf, A.M. Salem, G.B. Sakr, Chemically deposited Ni-doped CdS nanostructured thin films: Optical analysis and current-voltage characteristics. J. Alloys Compd. **776**, 1056–1062 (2019)

47. M. Mohamed, E.R. Shaaban, M.N. Abd-el Salam, A.Y. Abdel-Latief, S.A. Mahmoud, M.A. Abdel-Rahim, Investigation of the optical and electrical parameters $As_{47.5}Se_{47.5}Ag_5$ of thin films with different thicknesses for optoelectronic applications. Optik **178**, 1302–1312 (2019)

48. S.H. Wemple, Refractive index behavior of amorphous semiconductors and glasses. Phys. Rev. B **7**, 3767 (1973)

49. S.H. Wemple, M. DiDomenico Jr., Behavior of the electronic dielectric constant in covalent and ionic materials. Phys. Rev. B **3**, 1338 (1971)

50. A.S. Hassanien, Studies on dielectric properties, opto-electrical parameters and electronic polarizability of thermally evaporated amorphous $Cd_{50}S_{50-x}Se_x$ thin films. J. Alloys Compd. **671**, 566–578 (2016)

51. I.M. El Radaf, T.A. Hameed, G.M. El komy, T.M. Dahy, Synthesis, structural, linear and nonlinear optical properties of chromium doped SnO_2 thin films. Ceram. Int. **45**, 3072–3080 (2019)

52. A. El-Denglawey, M.M. Makhlouf, M. Dongol, The effect of thickness on the structural and optical properties of nano Ge-Te-Cu films. Results in Physics **10**, 714–720 (2018)

53. T. Wada, T. Maeda, Optical properties and electronic structures of $CuSbS_2$, $CuSbSe_2$, and $CuSb (S_{1-x}Se_x)_2$ solid solution. Phys. Status Solidi C **14**, 1600196 (2017)

54. A.S.M. Ahmad, R. Shakil, K. Uzma, A. Zahid, A. Afzal, K.A. Mahmood, masour, Appl. Phys. A. (2019) 14–17.

55. M. Shkir, V. Ganesh, S. AlFaify, I.S. Yahia, H.Y. Zahran, Tailoring the linear and nonlinear optical properties of NiO thin films through Cr^{3+} doping. J. Mater. Sci **29**, 6446–6457 (2018)

56. I.M. El Radaf, Structural, optical, optoelectrical and photovoltaic properties of the thermally evaporated Sb_2Se_3 thin films, Applied PhysicsL A Mater. Sci. Process. 125 (2019).

57. I.M. El Radaf, Structural, optoelectrical, linear, and nonlinear optical characterizations of the $Cu_2ZnGeSe_4$ thin films. J. Mater. Sci. **31**, 3228–3237 (2020)

58. A.S. Awed, N.A. El-Ghamaz, M.M. El-Nahass, H.M. Zeyada, Linear and nonlinear optical properties of alizarin red S thin films. Indian J. Phys. **93**, 861–868 (2019)

59. R.M. Abdelhameed, I.M. El Radaf, Self-cleaning lanthanum doped cadmium sulfide thin films and linear/nonlinear optical properties. Mater. Res. Express **5**, 66402 (2018)

60. I.M. El Radaf, R.M. Abdelhameed, Surprising performance of graphene oxide/tin dioxide composite thin films. J. Alloys Compd. **765**, 1174–1183 (2018)

61. S.R. Alharbi, A.A.A. Darwish, S.E. Algarni, H.I. ElSaeedy, K.F.A. El-Rahman, Influence of thickness and annealing on linear and nonlinear optical properties of manganese(III) chloride tetraphenyl porphine (MnTPPCl) organic thin films. Infrared Phys. Technol. **78**, 77–83 (2016)

62. G. Golan, A. Axelevitch, B. Gorenstein, V. Manevych, Hot-probe method for evaluation of impurities concentration in semiconductors. Microelectronics J. **37**, 910–915 (2006)

63. A.S. Hassanien, A.A. Akl, Effect of Se addition on optical and electrical properties of chalcogenide CdSSe thin films. Superlatt. Microstruct. **89**, 153–169 (2016)